Materials Today Bio 16 (2022) 100363

Contents lists available at ScienceDirect

Materials Today Bio

journal homepage: www.journals.elsevier.com/materials-today-bio

4D-printed bilayer hydrogel with adjustable bending degree for enteroatmospheric fistula closure

Guiwen Qu [a], Jinjian Huang [a], Ze Li [b], Yungang Jiang [a], Ye Liu [a], Kang Chen [b], Ziyan Xu [b], Yun Zhao [c], Guosheng Gu [a], Xiuwen Wu [a,b,**], Jianan Ren [a,b,*]

[a] Research Institute of General Surgery, Jinling Hospital, School of Medicine, Southeast University, Nanjing, 210009, China
[b] School of Medicine, Nanjing University, Nanjing, 210093, China
[c] Department of General Surgery, BenQ Medical Center, The Affiliated BenQ Hospital of Nanjing Medical University, Nanjing, 210019, China

ARTICLE INFO

Keywords:
4D printing
Shape morphing
Hydrogel
Enteroatmospheric fistula
Plugging technique

ABSTRACT

Recently, four-dimensional (4D) shape-morphing structures, which can dynamically change shape over time, have attracted much attention in biomedical manufacturing. The 4D printing has the capacity to fabricate dynamic construction conforming to the natural bending of biological tissues, superior to other manufacturing techniques. In this study, we presented a multi-responsive, flexible, and biocompatible 4D-printed bilayer hydrogel based on acrylamide-acrylic acid/cellulose nanocrystal (AAm-AAc/CNC) network. The first layer was first stretched and then formed reversible coordination with Fe^{3+} to maintain this pre-stretched length; it was later combined with a second layer. The deformation process was actuated by the reduction of Fe^{3+} to Fe^{2+} in the first layer which restored it to its initial length. The deformation condition was to immerse the 4D construct in sodium lactate (LA-Na) and then expose it to ultraviolet (UV) light until maximal deformation was realized. The bending degree of this 4D construct can be programmed by modifying the pre-stretched lengths of the first layer. We explored various deformation steps in simple and complex constructs to verify that the 4D bilayer hydrogel can mimic the curved morphology of the intestines. The bilayer hydrogel can also curve in deionized water due to anisotropic volume change yet the response time and maximum bending degree was inferior to deformation in LA-Na and UV light. Finally, we made a 4D-printed bilayer hydrogel stent to test its closure effect for enteroatmospheric fistulas (EAFs) *in vitro* and *in vivo*. The results illustrate that the hydrogel plays a role in the temporary closure of EAFs. This study offers an effective method to produce curved structures and expands the potential applications of 4D printing in biomedical fields.

1. Introduction

Enteroatmospheric fistula (EAF) is defined as an abnormal communication between the gastrointestinal tract and external atmosphere without overlaying soft tissue [1–3]. It is a severe complication following open abdomen as a result of the exposure of abdominal viscera [2], with a mortality rate up to 35% [4]. Damaged intestinal continuity leads to leakage of intestinal contents which delays spontaneous closure of the fistula [1,5]. The EAF closure remains a major challenge to be dealt with consequently. To date, there have been various techniques to control enteric effluent, such as self-expanding metal stents [6], silica gel patches [7], percutaneous endoscopic gastrostomy tube [8], silicone fistula plug [9], baby bottle nipples [10], and three-dimensional (3D)-printed thermoplastic polyurethane (TPU) stents [11]. However, these techniques may cause mechanical damage to the intestinal mucosa [12] and have trouble fitting the changeable bending structure of the bowels.

Hydrogels are a type of fascinating materials and can be used in various fields, including biologic scaffolds [13], tissue engineering [14,15], drug delivery [16], electronic devices [17–19], etc. Furthermore, the emergence of 3D printing offers an opportunity for the fabrication of hydrogels with customized shapes [13,20]. As research progresses, four-dimensional (4D) printing which integrates the fourth dimension, “time”, with 3D printing [21–24], has attracted attention of researchers [25]. It can overcome the major drawback of 3D printing considering only the initial status of printed objects [21,23], and therefore mimics the sophisticated dynamic structures of living tissues [26,27]. For instance,

* Corresponding author. Research Institute of General Surgery, Jinling Hospital, School of Medicine, Southeast University, Nanjing, 210009, China.
** Corresponding author. Research Institute of General Surgery, Jinling Hospital, School of Medicine, Southeast University, Nanjing, 210009, China.
E-mail addresses: wuxiuwen@nju.edu.cn (X. Wu), jiananr@gmail.com, Jiananr@nju.edu.cn (J. Ren).

https://doi.org/10.1016/j.mtbio.2022.100363
Received 8 April 2022; Received in revised form 15 June 2022; Accepted 9 July 2022
Available online 14 July 2022

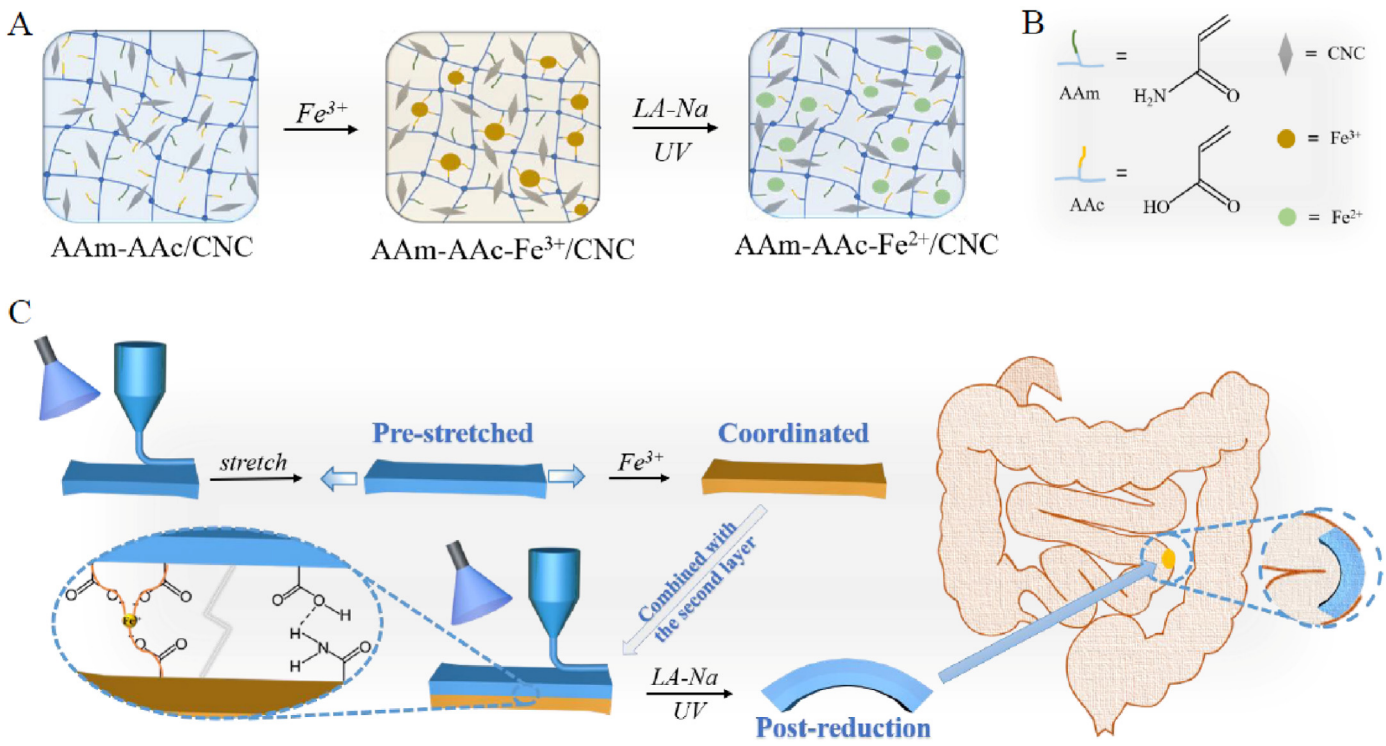

Fig. 1. (A) Schematic showing different phases of the first layer. (B) The molecular formula of chemical compositions used in this study. (C) Schematic showing 4D printing process of the bilayer hydrogel and its application.

Soon Hee Kim et al. presented a bilayer Sil-MA hydrogel deformed by anisotropic volume change due to different swelling behavior in aqueous solution to make trachea mimetic tissue [28]. Wang et al. utilized a NIR light-sensitive 4D ink material to simulate and reconstruct the curved topology of myocardial tissue for seamless integration [29]. Therefore, 4D printing of implants that conform to biological curvature can be a potential technology for reconstitution of defective organs and tissues. Various 4D printing strategies have been applied for the manufacture of surgical implants on recent trends, such as bone scaffolds [30,31], tracheal stents [28,32], and cardiac patches [29]. Their deformation mainly depends on two types of materials: (i) shape memory polymers (SMPs), such as thermo-sensitive polycaprolactone-based composites [32]; (ii) responsive shape morphing materials, such as 3D structures deformed by anisotropic swelling property distributed spatially [28]. Despite the fact that these materials can fit in tissue defects due to their shape change behaviors, they are still insufficient in quantitative control of programmed shapes.

Here, we fabricate a soft and flexible 4D-printed bilayer hydrogel with adjustable bending degree for EAF closure. The hydrogel we described here is composed of poly (acrylamide-co-acrylic acid) network and cellulose nanocrystals (CNCs). Metal cations can form coordination bonds with particular ligands, one type of noncovalent interaction essentially, which can regulate mechanical properties of biological materials [33,34]. For instance, Zheng et al. reported a hydrogel with high stiffness and toughness via the coordination between carboxyl and Fe^{3+} [34]. Moreover, the metal-ligand coordination bonds exhibit dynamic characteristics and can disaggregate under certain stimulations [34–37]. In our previous study, a color-variable and ultraviolet (UV)-sensitive electronic skin via reversible coordinated network between xanthan gum and Fe^{3+} was designed [35]. Inspired by this, we introduced ferric ion into the polymer network to act as a driving layer. Cellulose nanocrystals (CNCs) can be extracted from cellulose which is one of the most abundant biopolymers in nature [38]. They have attracted immense attractions in the field of biomaterials due to their high-cost performance, superior biocompatibility as well as excellent mechanical properties [39–41]. Here, we introduced CNCs into the network to improve print fidelity [42].

In total, we manufactured a bilayer hydrogel based on AAm-AAc/CNC network with Fe^{3+} ions added to the pre-stretched first layer to form reversible coordination with AAc so as to obtain shrinkage anisotropy when the bilayer construct was immersed in sodium lactate (LA-Na) solution and then exposed to UV light. Since the shape programming can be controlled quantitatively by pre-stretching the first layer to different lengths, the bilayer hydrogel can modify bending degree to realize seamless plugging of EAFs as the position requires (Fig. 1C). Additionally, the bilayer construct can also curve in deionized water due to anisotropic volume change.

2. Materials and methods

2.1. Reagents and materials

Acrylamide (AAm), 2-hydroxy-4'-(2-hydroxyethoxy)-2methyl-propiophenone (I-2959), cellulose nanocrystal (CNC), and urethane were purchased from Sigma-Aldrich, USA. Ferric chloride ($FeCl_3$), sodium hydroxide, DL-lactic acid, and hydrochloric acid (HCl) were obtained from Sinopharm Chemical Reagent Co., Ltd, China. Methylene-bis-acrylamide (MBA) and acrylic acid (AAc) were purchased from Aladdin Co., Ltd, China. The sodium lactate (LA-Na) solution (0.5 mol/mL) used in this study was prepared by adding 1.87 mL lactic acid into 20 mL of 1 mol/L NaOH solution, and then neutralized to pH = 7 with HCl.

2.2. Preparation of AAm-AAc/CNC inks

CNC (6 wt% of H_2O) was first added to 30 mL deionized water and fully dissolved under ultrasonic wave. AAm (20 wt% of H_2O), AAc (2 wt % of H_2O), MBA (0.04 wt% of H_2O), and I-2959 (0.5 wt% of H_2O) were joined next. The mixture was then heated to 50 °C under water bath to make these components completely dissolved and evenly mixed.

2.3. Fabrication of bilayer hydrogel

The basic components of both layers are described in Section 2.2. (i) Formation of the first layer: The AAm-AAc/CNC ink was poured into a self-prepared cuboid silicone mold and then irradiated by UV light (365 nm, ~6.0 W/cm^2, model: UVPL-411, Yunhe Tech Co. Ltd., China) for 120 s for complete polymerization. Next, the resulting hydrogel was pre-stretched to specific lengths and soaked in 2.4% w/v $FeCl_3$ aqueous solution for specific time to induce the coordination entirely between carboxylic groups in AAc and Fe^{3+} to fix the hydrogel at these specific lengths. The pre-stretched lengths and corresponding soaking time are listed in Table S1. The hydrogel was then transferred into deionized water and dialyzed for 3 h with six rounds of water refresh to remove uncross-linked components. This hydrogel was recorded as AAm-AAc-Fe^{3+}/CNC. (ii) Formation of the second layer: The pre-stretched first layer was placed in another suitable self-prepared cuboid silicone mold and the second layer of AAm-AAc/CNC ink was then added above to cover the surface. The entire area was polymerized under UV irradiation. Thus, the bilayer hydrogel was produced whose two-tier structures were connected tightly after UV irradiation. (iii) De-coordination of first layer: The resulting hydrogel in Step (i) was immersed in LA-Na for 3 min and then exposed to UV light for 5–20 min. The de-coordinated hydrogel was recorded as AAm-AAc-Fe^{2+}/CNC at its post-reduction state. Subsequent deformation tests were conducted by immersing the obtained bilayer hydrogel in Step (ii) in LA-Na for 3 min and then exposing it to UV light for 5–20 min until maximal deformation was realized.

2.4. Characterization

2.4.1. Microstructure

The samples of AAm-AAc/CNC, AAm-AAc-Fe^{3+}/CNC, and AAm-AAc-Fe^{2+}/CNC hydrogels were freeze-dried, sectioned vertically, and gold sputter-coated for observation under a scanning electron microscopy (SEM, Hitachi, Japan) at a voltage of 5 kV.

2.4.2. Fourier transform infrared spectroscopy (FTIR) measurements

The FTIR spectra of hydrogels were recorded by a Nicolet-6700 spectrometer (Thermo, USA) at room temperature with the wave number ranged from 4000 to 500 cm^{-1} via KBr pellet technique. The powders were ground to a dry KBr disk, and 32 scans at a resolution of 4 cm^{-1} were set to obtain the spectra.

2.4.3. Measurement of mechanical strength

The tensile, compressive, and adhesive properties of the hydrogels were measured via a universal material testing machine (MTS, model: CMT2103, USA). Hydrogel strips (20 mm long, 10 mm wide and 2 mm high) for tensile tests at 15 mm/min were made in customized molds. Hydrogel cylinders with a diameter of 5 mm, and a height of 6 mm were also produced in cylindrical molds for compression tests at 20 mm/min. The fracture energy (U) of hydrogels was calculated with the following Eq. (1) on the basis of the integral of the area under the tensile stress (τ)-strain (ε) curve:

$$U = \int \tau d\varepsilon \quad (1)$$

The adhesive properties of these hydrogels on intestines were investigated via lap shear adhesion tests. Porcine intestine was cut into pieces (4 cm × 1.5 cm), and hydrogel slices (1.5 cm × 1.5 cm) were placed between two pieces of porcine intestine (Fig. 3F). Then tensile forces were tested. Each mechanical test was performed three times.

2.4.4. Swelling behavior

Samples of AAm-AAc/CNC, AAm-AAc-Fe^{3+}/CNC, and AAm-AAc-Fe^{2+}/CNC hydrogels were prepared and freeze-dried. The dried weight was measured and recorded as W_d. These samples were then immersed in 2 mL deionized water. After a certain period of time, these samples were removed from deionized water, and the surface moisture was wiped with dust-free paper. After the weight was measured and recorded as W_s, they were returned to deionized water. This progress was repeated until an equilibrium swelling ratio was reached. The swelling ratio was calculated by the following Eq. (2) [43]:

$$\text{Swelling Ratio } (\%) = (W_s - W_d)/W_d \times 100 \quad (2)$$

2.4.5. Shear thinning property

The shear thinning properties of precursor solutions with 6% CNC or without CNC were measured with a rheometer (Anton Paar Co., Ltd, Austria) at shear rates from 0.1 to 500 s^{-1}.

2.5. 4D deformation of bilayer hydrogel

2.5.1. 4D deformation in deionized water

Bilayer hydrogels made by molds with the first layer pre-stretched to four-fold of the original length were soaked in deionized water for 48 h. Photos were taken every hour, and the bending degree at different times was recorded. The degree of bending was quantified by bending angle [44,45], and bending angle measurement is shown in Fig. S2A.

2.5.2. 4D deformation in LA-Na and UV light

Bilayer hydrogels same as above in Section 2.5.1 were immersed in LA-Na for 3 min and then exposed to UV light for 20 min to compare with the deformation in deionized water. Photos were taken every 3 min to record the bending degree.

Bilayer hydrogels with the first layer pre-stretched to particular lengths (two-, three-, and four-fold of the original length) were immersed in LA-Na for 3 min and then exposed to UV light for 5–20 min to observe the shape-morphing process. Corresponding photos were recorded when the constructs reached equilibrium state.

To explore more complex deformation of bilayer hydrogels, we designed cross-shaped bilayer hydrogels in self-prepared molds. The first layers of cross-shaped bilayer hydrogels were similarly pre-stretched to two-, three-, and four-fold of the original length along the two long axis directions. The cross-shaped hydrogels were also immersed in LA-Na and then irradiated by UV light to induce de-coordination step of the first layers. Photos were taken throughout the deformation process. The bending angle measurement of cross-shaped hydrogels is shown in Fig. S2B.

2.6. 4D printing process of bilayer hydrogel

A lab-tailored extrusion 3D printer with a nozzle diameter of 0.4 mm and a printing speed of 200 mm/min was utilized to print AAm-AAc/CNC inks. An additional UV point-light source was used to initiate polymerization. The STL. file of printed graphics was designed by Cinema 4D software.

2.7. Cytocompatibility study

L929 fibroblasts were cultivated for the biocompatibility test of AAm-AAc/CNC, AAm-AAc-Fe^{3+}/CNC, and AAm-AAc-Fe^{2+}/CNC hydrogels. Samples of these hydrogels were made and freeze-dried in advance. They were later soaked in cell culture medium and disinfected by ultraviolet irradiation for 24 h. The leachates and fibroblasts were seeded in a 24-well culture plate and co-cultured for 24 h and 48 h respectively. Cell viability was observed under a fluorescence microscope (Thermo Fisher Scientific Co., Ltd, USA) after stained by calcein AM and propidium iodide (PI).

2.8. Anti-enzymatic hydrolysis assay

AAm-AAc/CNC, AAm-AAc-Fe^{3+}/CNC, and AAm-AAc-Fe^{2+}/CNC

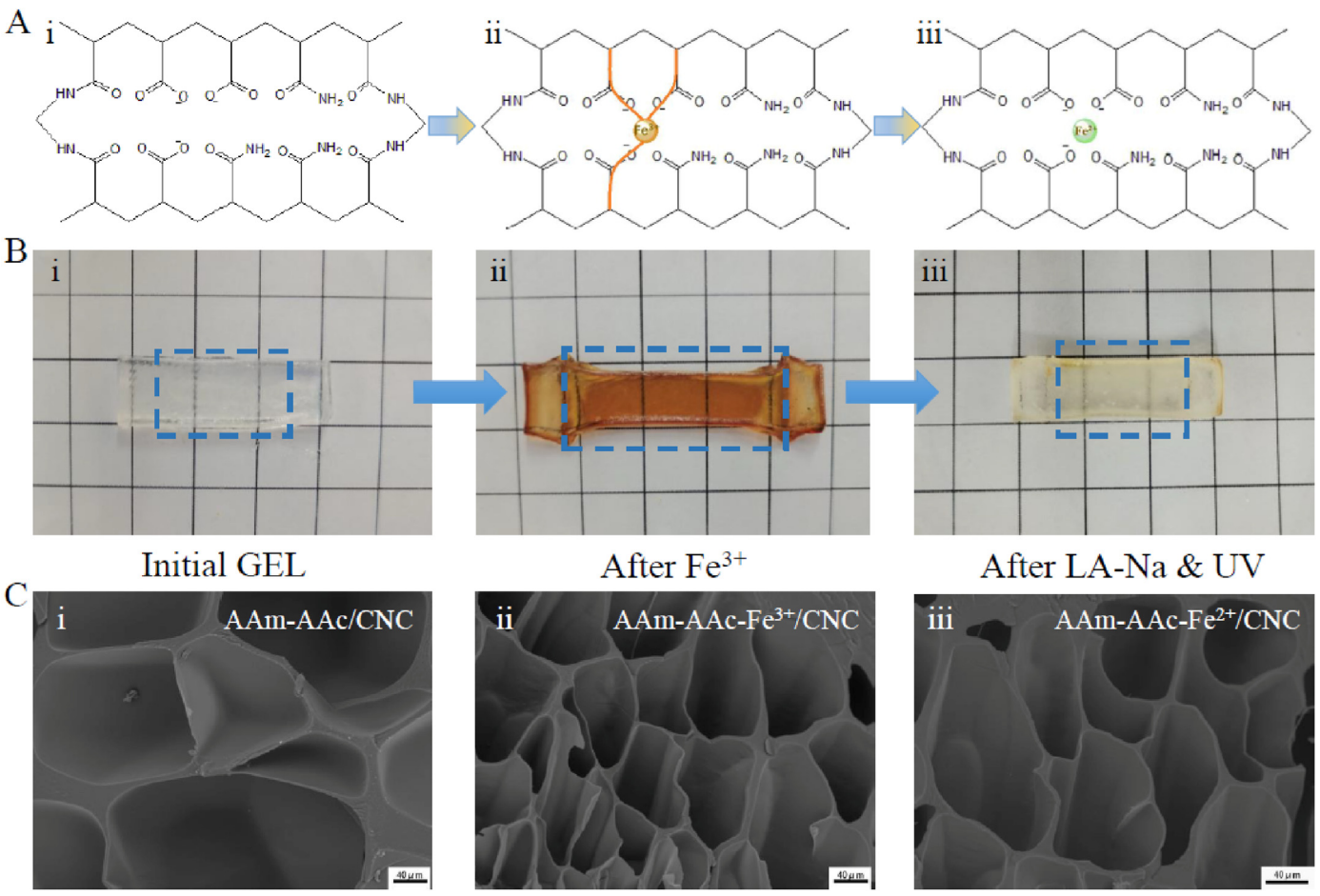

Fig. 2. Morphology and microstructure of hydrogels. (A) Hydrogel networks. (B) Physical photos of hydrogels. The size of the grid unit in the photo background is 1 cm by 1 cm. (C) The SEM morphology at the core area of hydrogels: (i) AAm-AAc/CNC, (ii) AAm-AAc-Fe^{3+}/CNC, (iii) AAm-AAc-Fe^{2+}/CNC. Scale bars: 40 μm.

hydrogels were prepared in cylindrical molds and frozen-dried. The initial weights were measured and recorded. Samples were then separately immersed in fresh intestinal juices in 37 °C. The intestinal juices were replaced every 12 h. The hydrogels were removed after 72 h. The moisture on the surface was wiped off using dust-free paper. The hydrogels were then again freeze-dried, weighed, and recorded.

2.9. *In vitro experiments of EAF closure*

Pieces of porcine intestines and a resin intestinal model printed by a digital light processing (DLP) 3D printer (Formlabs, USA) were utilized for this experiment. First, 10-cm porcine small intestine pieces equipped with a 2 mm hole were linked to a syringe pump allowing uniform perfusion of PBS and the other end was tied up to block flow. A pressure sensor was also connected to this model to measure the maximum pressure. Control group (without plugging measures), TPU group (plugged by a 3D-printed TPU stent), and Hydrogel group (plugged by a 4D-printed bilayer hydrogel) were observed. The TPU stents printed by a fused deposition modeling (FDM) 3D printer (Creality Co., Ltd, China) are used for EAFs closure in our previous reports [11,12,46]. PBS was pumped into this equipment at a uniform speed of 10 mL/min to simulate the flow of intestinal juice. Imaging data and the maximum pressure reading were recorded. Next, a resin intestinal model (20 mm in diameter) was used to simulate the human intestinal tract. The model had a 2-mm-diameter hole at the bend to mimic the orificium fistulae. We connected a syringe containing PBS with the resin model to simulate the outputs of EAFs. The output of three groups including Control group (without plugging measures), TPU group (plugged by a 3D-printed TPU stent), and Hydrogel group (plugged by a 4D-printed bilayer hydrogel) were observed. Imaging data were recorded during this process.

2.10. *In vivo animal experiments of EAF closure*

Nine male New Zealand white rabbits (4 months of age, weighed 2.5 ± 0.5 kg, provided by the Department of Comparative Medicine, Jinling Hospital) were conventional raised for one week and then randomly divided into three groups including Control group (without plugging measures), TPU group (plugged by a 3D-printed TPU stent) and Hydrogel group (plugged by a 4D-printed bilayer hydrogel). Preoperative blood was collected in advance via an ear vein. After fasting for one day, the rabbits underwent a terminal ileostomy connecting the ileum to the exterior. They were fixed in supine position with feet separated and abdomen shaved. Their abdomen was cut open along the linea alba and the ileum was identified. A section of the ileum was pulled outside the skin through a puncture in the left abdominal wall and sutured to the abdomen, thus minimizing damage to blood vessels. Next, the abdominal wall was closed and the exposed ileum was cut via a 2-cm incision to create an EAF model. The fistulas of rabbits in TPU group and Hydrogel group were plugged with 3D-printed TPU stents and 4D-printed bilayer hydrogels respectively, which were fixed outside abdomen by a 3D printed claw-shaped frame; the other three were treated as Control group without any interventions. During the procedure, rabbits were first injected urethane (1.2 g/kg) through the auricular vein to induce anesthesia. After 2 h, they accepted continuous anesthesia via micropump of pentobarbital sodium (10 mg/kg · h) for 4 h and then anesthetic dose was adjusted to 20 mg/kg · h. Postoperative parenteral nutrition, analgesics,

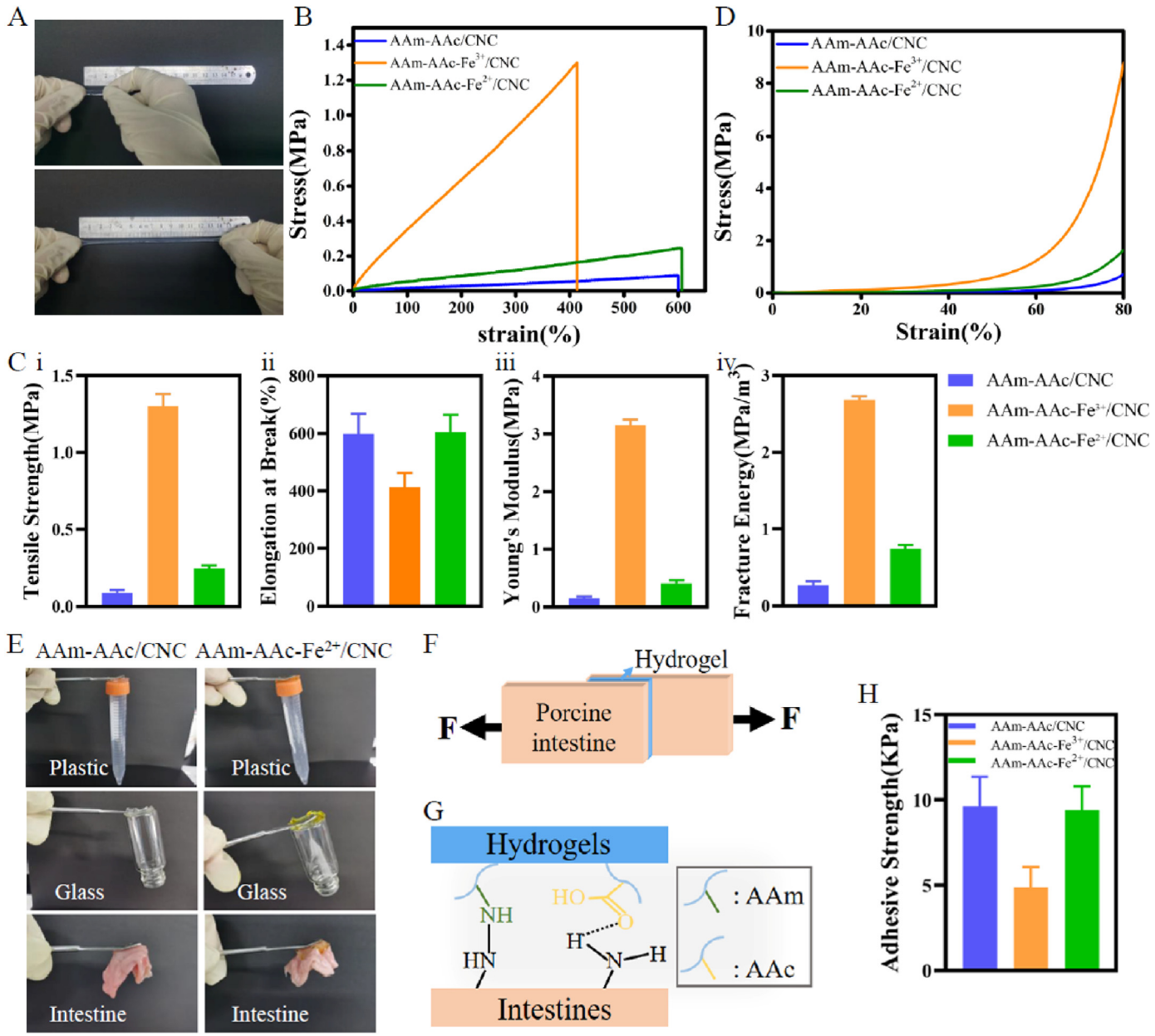

Fig. 3. Mechanical properties of hydrogels. (A) Tensile changes of hydrogels. (B) Tensile stress-strain curves of hydrogels. (C) (i) Tensile strength, (ii) Elongation at break, (iii) Young's modulus, and (iv) Fracture energy of hydrogels. (D) Compressive stress-strain curves of hydrogels. (E) Adhesion of the AAm-AAc/CNC hydrogel and AAm-AAc-Fe^{2+}/CNC hydrogel to inorganic surfaces and organic surface. (F) Schematic of lap shear adhesion tests. (G) Schematic of the adhesion between hydrogels and porcine intestines. (H) Adhesive strength of hydrogels on porcine intestine pieces was measured by lap shear adhesion tests.

and antibiotics were provided. All rabbits were placed in a warm room for a day and a half to observe and record the leakage of intestinal juice. The blood of these rabbits was collected again after the observation period. Rabbits were euthanized by i.v. injection of pentobarbital sodium when the experiment was completed. Plasma was extracted from blood samples by centrifugation. The serum levels of total protein (TP) and albumin (ALB) were determined by testing kits. All experiments were approved by the Animal Investigation Ethics Committee of Jinling Hospital.

3. Results and discussion

3.1. Fabrication of 4D shape-morphing bilayer hydrogel

Both layers of the hydrogels were obtained by UV crosslinking of AAm-AAc/CNC ink. The morphing process was driven by the first layer that introduced Fe^{3+} to the network. As shown in Fig. 1A, when the AAm-AAc/CNC hydrogel was stretched and immersed in ferric chloride solution, carboxylic groups among AAc can form coordination bonds with Fe^{3+} which made the network fixed at this stretched length. The combination was reversible. The coordination bonds can be destabilized due to the reduction of Fe^{3+} (from Fe^{3+} to Fe^{2+}) when the resulting AAm-AAc-Fe^{3+}/CNC hydrogel was immersed in LA-Na and then exposed to UV light—this in turn created shrinkage stress in the internal network that restored the hydrogel to its original position. The reduction process can be explained by the following chemical formulas (3) and (4) [35]:

$$\text{sodium lactate} = CH_3CH(OH)COONa \tag{3}$$

$$Fe^{3+} + CH_3CH(OH)COONa \xrightarrow{UV} Fe^{2+} + CH_3CH(OH)\cdot + Na^{+} + CO_2\uparrow \tag{4}$$

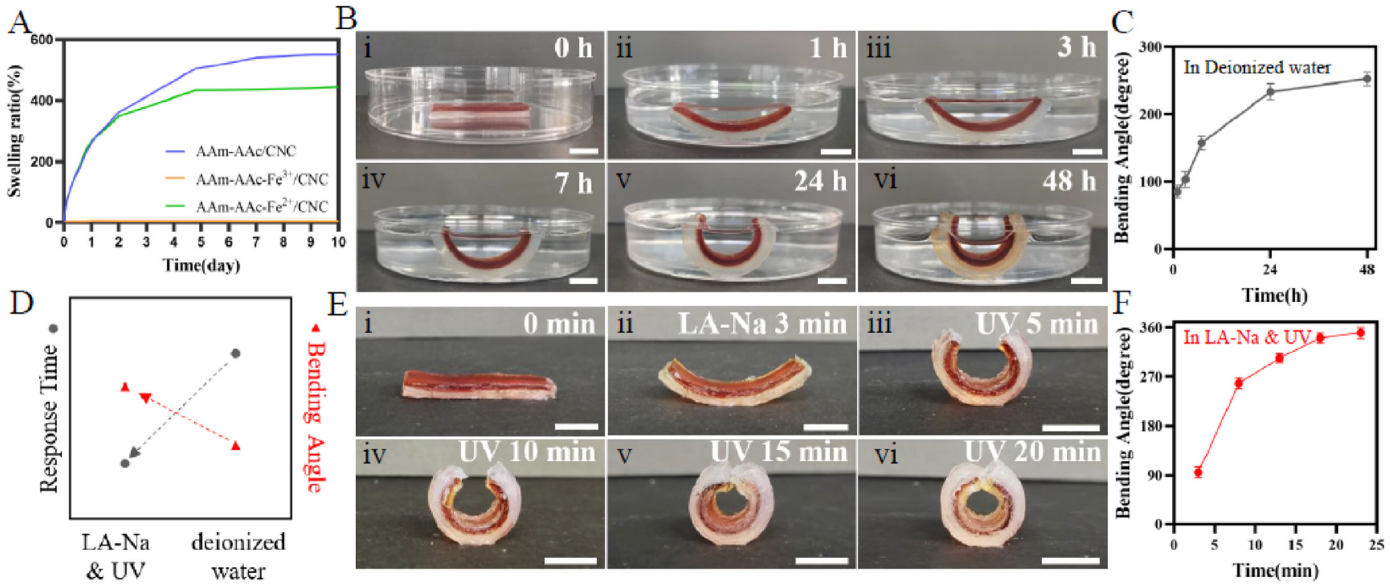

Fig. 4. (A) Swelling ratio of AAm-AAc/CNC, AAm-AAc-Fe^{3+}/CNC, and AAm-AAc-Fe^{2+}/CNC hydrogels. (B) 4D shape-morphing process in deionized water. (C) Change of bending angle in deionized water. (D) Comparison of response time and maximum bending angle in sodium lactate and UV with in deionized water. (E) 4D shape-morphing process in sodium lactate and UV. (F) Change of bending angle in sodium lactate and UV. Scale bars: 1 cm.

The physical photos of initial state, pre-stretched state, and post-reduction state of the first layer and corresponding internal network diagrams are shown in Fig. 2A and B; the results coincided with previous descriptions. The second layer contains a simple AAm-AAc/CNC network and served as a passive layer that remained constant in sodium lactate solution and under UV irradiation. We united the pre-stretched first layer with the second layer to create a 4D shape-morphing structure. The two layers were tightly connected owing to the formation of interpenetrating network and hydrogen bonds at the interface. The difference in shrinkage behavior actuated the hydrogel to curve when the bilayer hydrogel was immersed in LA-Na and then exposed to UV light.

3.2. Characterization of hydrogels

3.2.1. Microstructure

All hydrogels were porous, and the pore sizes shown in the SEM reflected the reversible ionic crosslinking in the microstructure. As shown in Fig. 2C, the AAm-AAc/CNC hydrogel revealed maximum pores. The hydrogel developed a microstructure with higher density and smaller pore size as the carboxyl groups in AAc formed ionic crosslinking with Fe^{3+}. Once Fe^{3+} in the hydrogels was reduced to Fe^{2+} after being immersed in LA-Na and irradiated by UV light, the pores were extended but still slightly smaller than those of the initial state perhaps due to the extra exposure to UV light which made the network closer.

3.2.2. Fourier infrared spectroscopy (FTIR) measurements

The FTIR spectra in Fig. S1 shows that the asymmetric and symmetric stretching vibrations of COO^- groups in AAc appeared at 1600 cm^{-1} and 1411 cm^{-1}. They shifted to 1603 cm^{-1} and 1412 cm^{-1} when combined with Fe^{3+}, and fell back to 1600 cm^{-1} and 1409 cm^{-1} when Fe^{3+} was reduced to Fe^{2+}. This result illustrates the coordination interaction between COO^- and ferric ion.

3.2.3. Mechanical properties of the hydrogels

Tensile and compression tests were conducted to confirm the impact of Fe^{3+} added in the hydrogels as well as changes in the mechanical performance due to subsequent valence variation. The AAm-AAc/CNC hydrogel can be slowly stretched up to nearly seven-fold compared to its original length (Fig. 3A), which provided foundation for further fabrication of the driving layer in the 4D-printed structure. The tensile stress-strain curves of hydrogels shown in Fig. 3B illustrated that the mechanical strength increased markedly after the AAm-AAc/CNC hydrogel was soaked in ferric chloride solution under which the AAm-AAc-Fe^{3+}/CNC hydrogel took shape. This change was largely due to the formation of the second network between iron ions and carboxyl groups in AAc. Fig. 3C shows that the coordination of AAc/Fe^{3+} increased tensile strength from ~0.089 MPa to ~1.3 MPa, increased Young's modulus from ~0.149 MPa to ~3.15 MPa, increased fracture energy from ~0.266 MPa/m^3 to ~2.68 MPa/m^3 and reduced elongation at break from ~599% to ~413%, which suggested that the AAc/Fe^{3+} coordination made the hydrogel more solid and fragile. When Fe^{3+} in the hydrogel was reduced to Fe^{2+}, the values mentioned above decreased but they were slightly higher than those of the initial state.

The compressive stress-strain curves of hydrogels showed that the coordination of AAc/Fe^{3+} increased the compression strength in agreement with the results of tensile test (Fig. 3D). These results indicate that all of these hydrogels possessed good tensile and compressive capability, and could prepare a plugging stent for EAFs.

Besides the satisfactory tensile and compressive properties, the AAm-AAc/CNC hydrogel and AAm-AAc-Fe^{2+}/CNC hydrogel exhibited good adhesion capacity to organic surfaces including plastic and glass as well as inorganic surfaces including porcine intestines (Fig. 3E). The coordination of AAc/Fe^{3+} decreased the adhesion property, as the adhesive strength of AAm-AAc-Fe^{3+}/CNC hydrogel (~5 KPa) was lower than that of AAm-AAc/CNC hydrogel (~9.6 KPa) and AAm-AAc-Fe^{2+}/CNC hydrogel (~9.4 KPa) (Fig. 3H). The adherence mechanism of these hydrogels on porcine intestine is clarified in Fig. 3G, that carboxyl groups and amino groups in AAm and AAc can form interfacial bonds with intestinal tissues, such as hydrogen bonds and nitro bonds. This characteristic enables the bilayer hydrogel to adhere to the intestines around EAFs.

3.3. 4D deformation of bilayer hydrogel

3.3.1. Deformation caused by swelling anisotropy in deionized water

The swelling behavior of these three hydrogels shown in Fig. 4A presented the swelling differences in deionized water. The AAm-AAc/CNC and AAm-AAc-Fe^{2+}/CNC hydrogel were similar in swelling rate in the first two days; later, the AAm-AAc/CNC hydrogel showed a higher swelling ratio due to its broader pores in microstructure. The AAm-AAc-

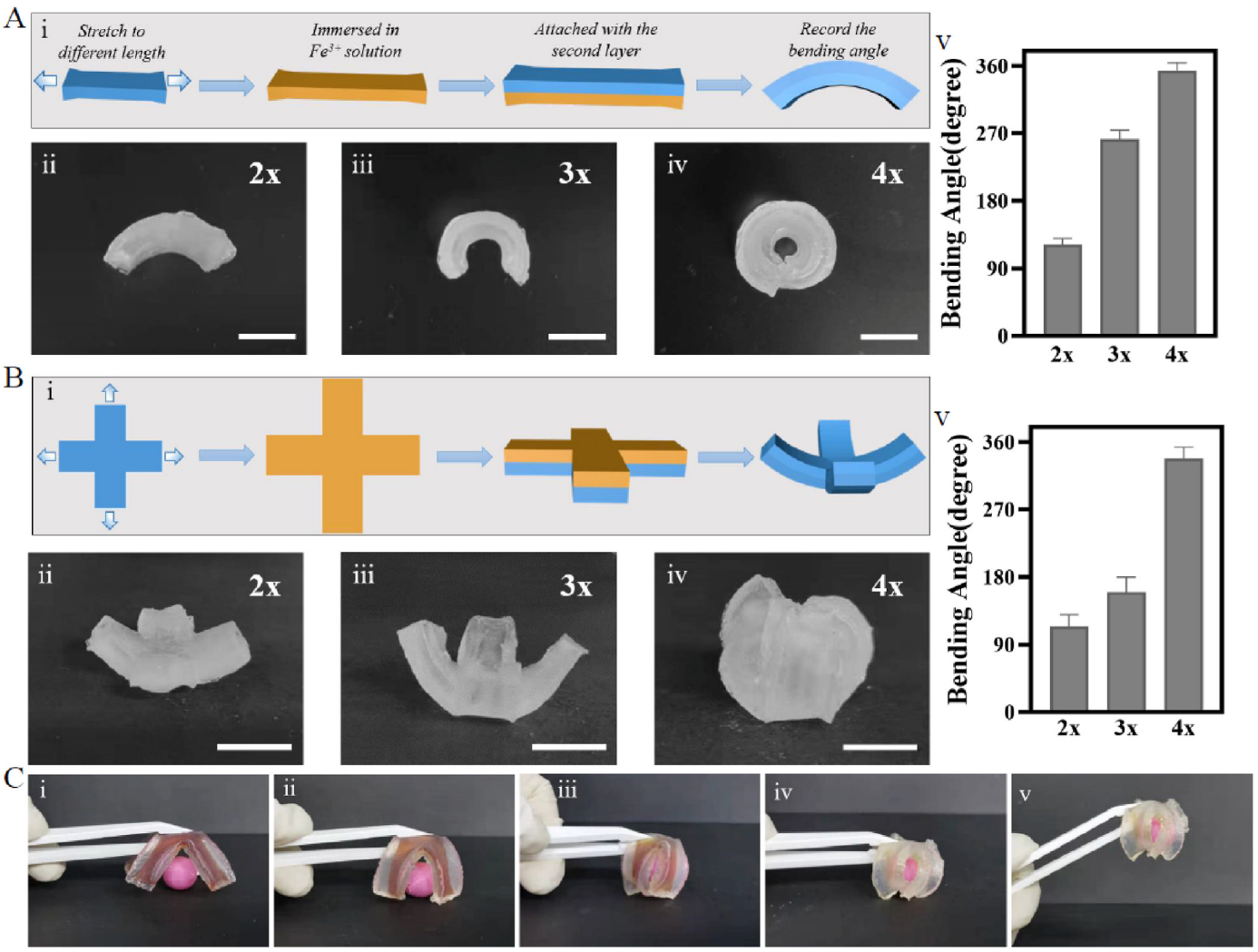

Fig. 5. Shape-morphing architecture by mold manufacturing. (A) (i) Schematic of shape-morphing process in bilayer hydrogel strips. (ii–iv) Photograph of hydrogel strips showing curled structures with different bending degrees programmed by different pre-stretched lengths of the first layer. (v) Corresponding bending angle with different pre-stretched lengths in hydrogel strips. (B) (i) Schematic of shape-morphing process of cross-shaped bilayer hydrogels. (ii–iv) Photograph of cross-shaped hydrogels showing curled structures with different bending degrees programmed by different pre-stretched lengths of the first layer along the two long axis directions. (v) Corresponding bending angle with different pre-stretched lengths in cross-shaped hydrogels. (C) Photograph of cross-shaped bilayer hydrogel grabbing a bead. Scale bars: 1 cm.

Fe^{3+}/CNC hydrogel was almost non-swollen in deionized water as a result of its very high crosslinking density [47]. The swelling behavior is in general accord with the pore size in hydrogels [48].

We next prepared bilayer hydrogel strips with the first layer pre-stretched to four-fold of the original length in a silicone mold and tested deformation behavior due to the swelling anisotropy of two layers in deionized water. Fig. 4B(i–vi) shows that the initial straight shape of a bilayer hydrogel gradually began to bend in deionized water. The bending degree was quantified in Fig. 4C. The bending angle of bilayer hydrogel reached ~252° at 48 h. No separation of the bilayer structure was observed during this process.

3.3.2. *Deformation caused by shrinkage anisotropy in LA-Na and UV light*

The deformability of the bilayer hydrogel sample same as above after being immersed in LA-Na and irradiated by UV was explored in Fig. 4E(i-vi). The straight structure had a bending angle of ~95° after being immersed in LA-Na for 3 min. The sample was later exposed to UV radiation, and the bending degree gradually increased and reached a maximum of ~350° at 20 min (Fig. 4F). Likewise, there was no delamination between the two layers. The deformation process in LA-Na and UV light was presented in Supplementary Video 1 and Supplementary Video 2.

Supplementary video related to this article can be found at doi:10.1016/j.mtbio.2022.100363

We next compared response duration and maximum bending angle of the same bilayer hydrogel in deionized water with in LA-Na and UV light. The response time to maximum bending degree in LA-Na and UV light was ~20 min, which is much faster than in deionized water (~48 h). Moreover, the maximum bending angle in LA-Na and UV light was also higher than in deionized water (Fig. 4D). Therefore, subsequent work used LA-Na and UV light as stimulus condition for 4D deformation.

3.4. *Shape-morphing architecture by mold manufacturing*

To systematically analyze the shape-morphing behaviors in LA-Na followed by UV irradiation, we next fabricated three types of bilayer hydrogels with the first layer pre-stretched to different lengths. In the first layer, AAm-AAc/CNC hydrogel networks were pre-stretched to two-, three-, and four-fold of the original lengths and then fixed with Fe^{3+}. The second layer was AAm-AAc/CNC hydrogel with the same length as the first layer after being pre-stretched. The bilayer layer was then soaked in LA-Na and exposed to UV light. During this process, the bonds between carboxyl groups and Fe^{3+} unlocked leading to an anisotropic contractile

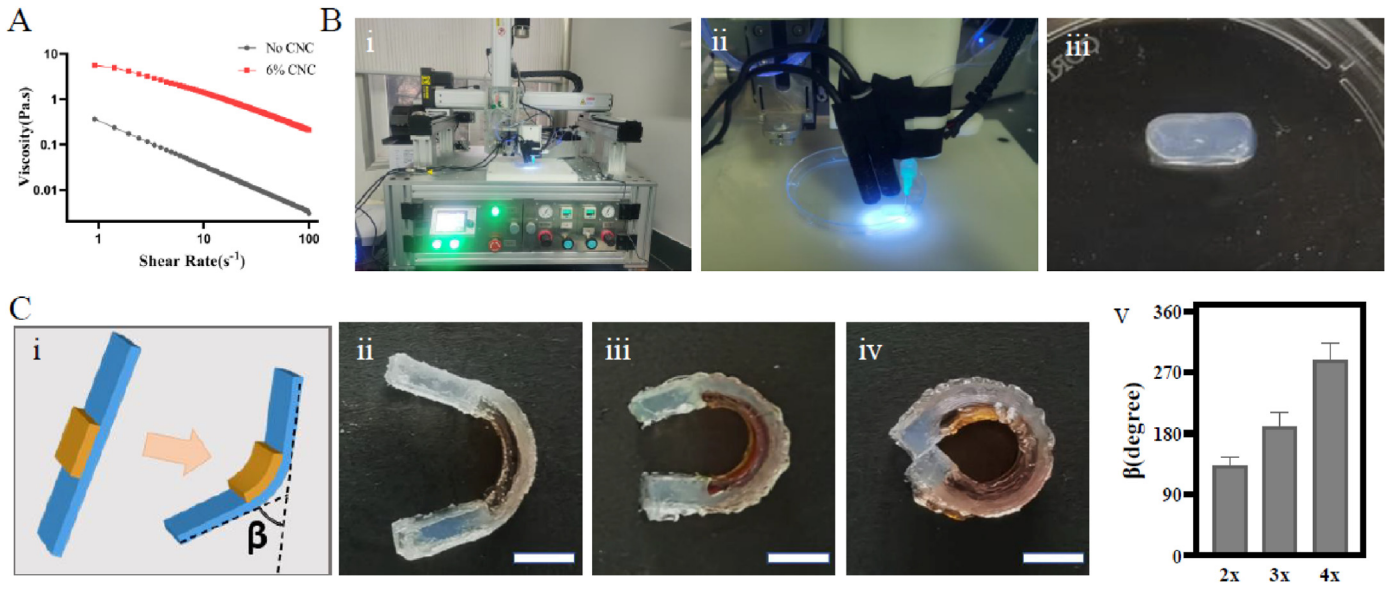

Fig. 6. 4D printing of shape morphing hydrogels. (A) Shear thinning property of precursor ink with or without CNC. (B) (i) The platform for printing. (ii) The 3D printing process as used for hydrogel strip. (iii) The 3D-printed hydrogel strip. (C) Shape-folding of a 4D-printed bilayer hydrogel composite film: (i) schematic; (ii-iv) shape-folding process; (v) column of the folding angle with different pre-stretched lengths of the first layer. Scale bars: 1 cm.

force between two layers, which contributed to the shape transformation as shown in Fig. 5A(i). Fig. 5A(ii–iv) presented different bending degrees under different pre-stretched lengths of the first layer. The bend degree raised with increased pre-stretched lengths. When the initial length of the first layer was pre-stretched to two-, three-, and four-fold, the bending angle reached ~122°, ~262° and ~354° respectively. As a result, we can obtain various bending degrees in the bilayer hydrogels through pre-stretching the first layer to different lengths.

We next produced cross-shaped bilayer hydrogels for testing to further explore the effect of pre-stretched level of the first layer on the integral bending of bilayer hydrogel. Fig. 5B(i) shows that the first layer was also pre-stretched to two-, three-, and four-fold of original length along the two long axis directions. The bending degree similarly increased consistent with the pre-stretched level as shown in Fig. 5B(ii–iv). The corresponding bending angles of the first layer pre-stretched to two-, three-, and four-fold of the original lengths were ~114°, ~160°, and ~338°. Moreover, an UV-activated gripper was designed to observe the curving of cross-shaped bilayer hydrogel more intuitively. The bilayer gripper with the first layer pre-stretched to four-fold of the original was soaked in LA-Na for 3 min in advance. The sample was then clamped with tweezers and exposed to UV light. Its arms bent toward the red bead gradually, and ultimately grasped the bead to lift the bead up (Fig. 5C).

3.5. 4D-printed shape-morphing architecture

First, to make 4D-printed hydrogel scaffolds with high shape fidelity, the printability of the ink was tested to determine the optimal printing factor. As shown in Fig. 6A, the precursor solution containing 6% CNC possessed preferable shear thinning behavior to the solution without CNC. Thus, we next selected the ink consisting of 6% CNC for 4D-printed hydrogel manufacturing.

The 3D printer employed here is shown in Fig. 6B (i). The printing process and a printed regular model were described in Fig. 6B(ii, iii). Three-dimensional printing was used to fabricate another bilayer structure in which the first layer was partly covered by the second layer (Fig. 6C). The folding angle can be modified by controlling the pre-stretched length of the first layer. As the printed first layer was pre-stretched to two-, three-, and four-fold of the original length, the folding angle were ~132°, ~189° and ~287° accordingly, thus suggesting that the folding angle increased consistent with the pre-stretched ratio of the first layer.

3.6. In vitro experiments of cytocompatibility, anti-enzymatic hydrolysis property and EAF closure

The cytocompatibility of these hydrogels was evaluated by co-culture of leachates with L929 fibroblasts. Fibroblasts developed nicely in the medium after 24 h and 48 h in all groups. Dead cells (marked as red) were rarely observed (Fig. 7A). Furthermore, the viability of cells co-cultured with AAm-AAc/CNC, AAm-AAc-Fe^{3+}/CNC, and AAm-AAc-Fe^{2+}/CNC hydrogels leachates all exceeded 95% with no significant difference versus cultured in medium (Fig. 7B). The results proved that all these hydrogels had great biocompatibility.

Moreover, these hydrogels were resistant to enzymatic hydrolysis, they swelled slightly after being immersed in intestinal juice for 72 h with no noticeable volume loss (Fig. S3). The results suggest that the bilayer hydrogel can work well in the gut environment.

We then took pieces of porcine intestines for perfusion and pressure testing to demonstrate the plugging effect of the 4D-printed bilayer hydrogel. There was no PBS leaking with the existence of bilayer hydrogel. The broken porcine intestine plugged with the bilayer hydrogel can withstand maximum pressure up to ~9.8 KPa, significantly higher than those of control group (~0.5 KPa) and TPU group (~4.5 KPa) (Fig. 7C). The effective result of the bilayer hydrogel is mainly due to its good adhesive performance to porcine intestines.

Next, a resin intestinal model with a hole was prepared by a DLP 3D printer to further test the plugging effect of the hydrogel. With the closure by a 4D-printed bilayer hydrogel, no PBS flowed out in stark contrast to the outcome of Control group and TPU group as shown in Fig. 7D (i–vi). The result illustrates that the 3D-printed TPU stent can hardly fit the curved intestinal model. In addition, the photos in Fig. S4 confirm that the bilayer hydrogel with a definite bending degree can nicely fit the intestinal model.

3.7. In vivo experiments of EAF closure

We next established an EAF model with rabbits to evaluate the effects of closing EAFs using 4D-printed bilayer hydrogel *in vivo*. The surgical procedure of modeling EAFs and the implantation of 4D-printed bilayer

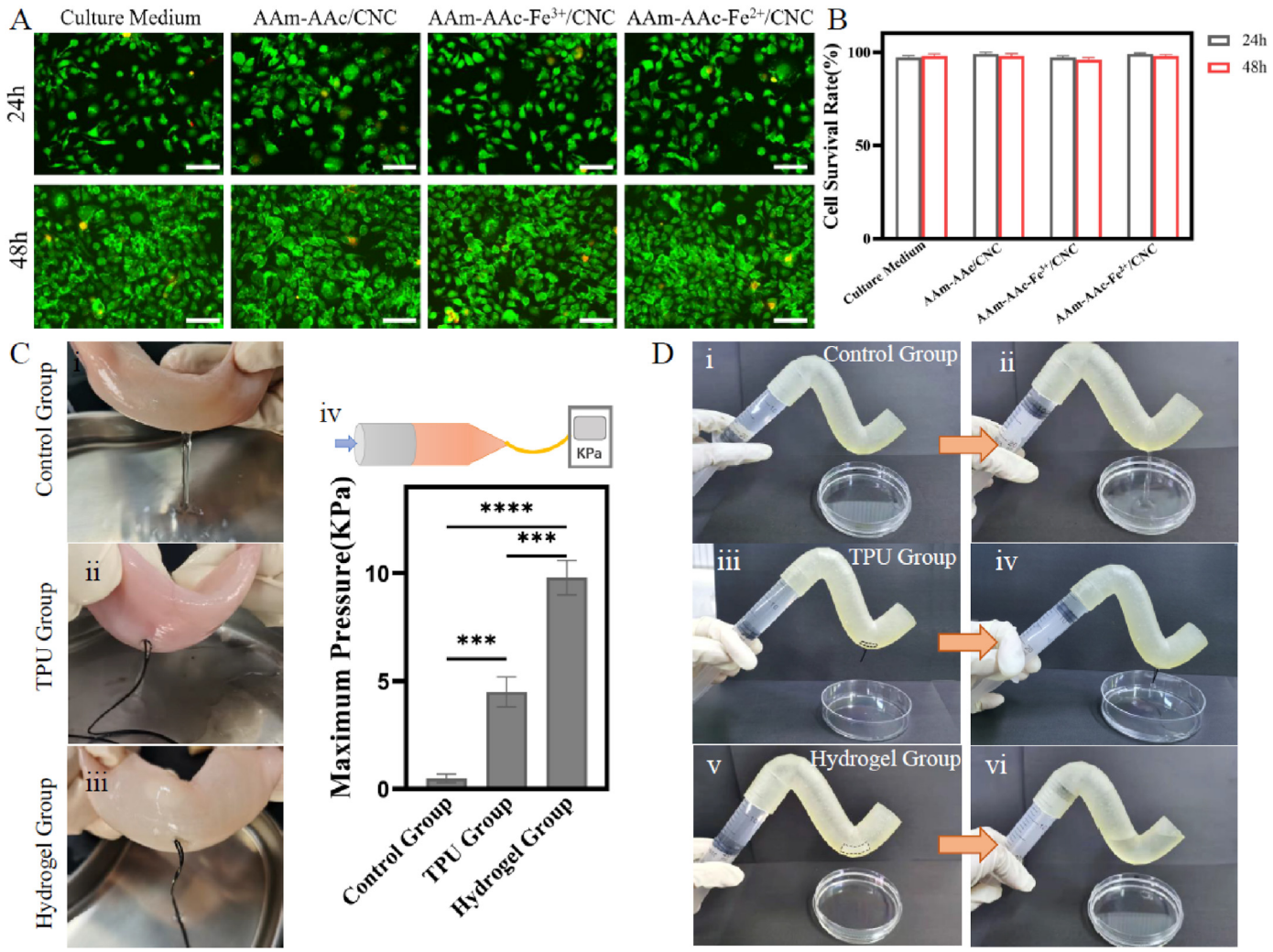

Fig. 7. *In vitro* experiments. (A) Live/dead assay of L929 fibroblasts co cultured with hydrogel leachates at 24 h and 48 h. Scale bars: 100 μm. (B) Live cell count at 24 h and 48 h. (C) Plugging effect of bilayer hydrogel in porcine intestinal with a 2-mm hole: (i) Control group (without plugging measures); (ii) TPU group (plugged by a 3D-printed TPU stent); (iii) Hydrogel group (plugged by a 4D-printed bilayer hydrogel); (iv) maximum pressure that the intestine can bear. ***$p < 0.001$, ****$p < 0.0001$, statistical analysis using one-way ANOVA. (D) Plugging effect of bilayer hydrogel in a resin intestinal model with a 2-mm hole: (i-ii) Control group (without plugging measures); (iii-iv) TPU group (plugged by a 3D-printed TPU stent); (v-vi) Hydrogel group (plugged by a 4D-printed bilayer hydrogel).

hydrogel are shown in Fig. 8A. The 4D-printed bilayer hydrogel stent and 3D-printed TPU stent used here are shown in Fig. S5, and they were tightly fixed to the intestinal wall with surgical sutures tying to claw-shaped frames. This study focused primarily on the temporary closure of EAFs, and thus the observation window was set to 36 h after operation. The leakage of intestinal effluents was the most intuitive indicator to reflect the closure effect. Fig. 8B shows that total leakage of intestinal juice can be up to ~289 mL when no measure was taken to close the EAF. The application of TPU stents reduced the leakage to ~206 mL, but was still higher than that of Hydrogel group (~63 mL). This result suggests that 3D-printed TPU stents lack tight adhesion to intestinal walls, and can hardly fit the bowel shape of target fistulas as well. The hydrogel group which placed 4D-printed bilayer hydrogel stents demonstrated great closure effect. The black arrow indicated the abscission of the bilayer stent in one rabbit after which the leakage volume increased substantially. The fistula output of the other two rabbits in this group had no obvious increase. This result suggested that the 4D-printed bilayer hydrogel stent had positive effects on the temporary prevention of intestinal juice overflow in EAFs.

The fistula output can cause low nutrition in the body [3,49], and thus the total protein (TP) and albumin (ALB) of rabbits were detected before treatment and after intervention. From the columns in Fig. 8C and D, TP and ALB values in rabbits treated with 4D-printed stents outperformed remarkably in Control group and TPU group. The slight difference between Hydrogel group with pre-operation state was attributed to the abscission of the stent in that rabbit in later-stage. The results suggest that the 4D-printed bilayer hydrogel stent took effect in the prevention of output in EAFs, which in turn lead to better nutritional status. We propose that this bilayer hydrogel stent can be replaced every 36 h to achieve continuous closure clinically in order to maintain patient nutritional status until spontaneous closure or surgical restoration of intestinal continuity are realized.

4. Conclusion

In this study, we proposed a novel strategy to manufacture 4D-printed multi-responsive bilayer hydrogels. Our results illustrated that the material possesses excellent mechanical properties and good biocompatibility. It offers controllable bending degree to completely fit the curved intestine, thus leading to seamless closure of EAFs. To our knowledge, this is the first try to utilize 4D printing technique for the treatment of EAFs. This study also provides a simple and convenient technique to fabricate flexible and curved 4D architectures, which in turn will further enlighten the exploration of 4D-induced structures for clinical applications.

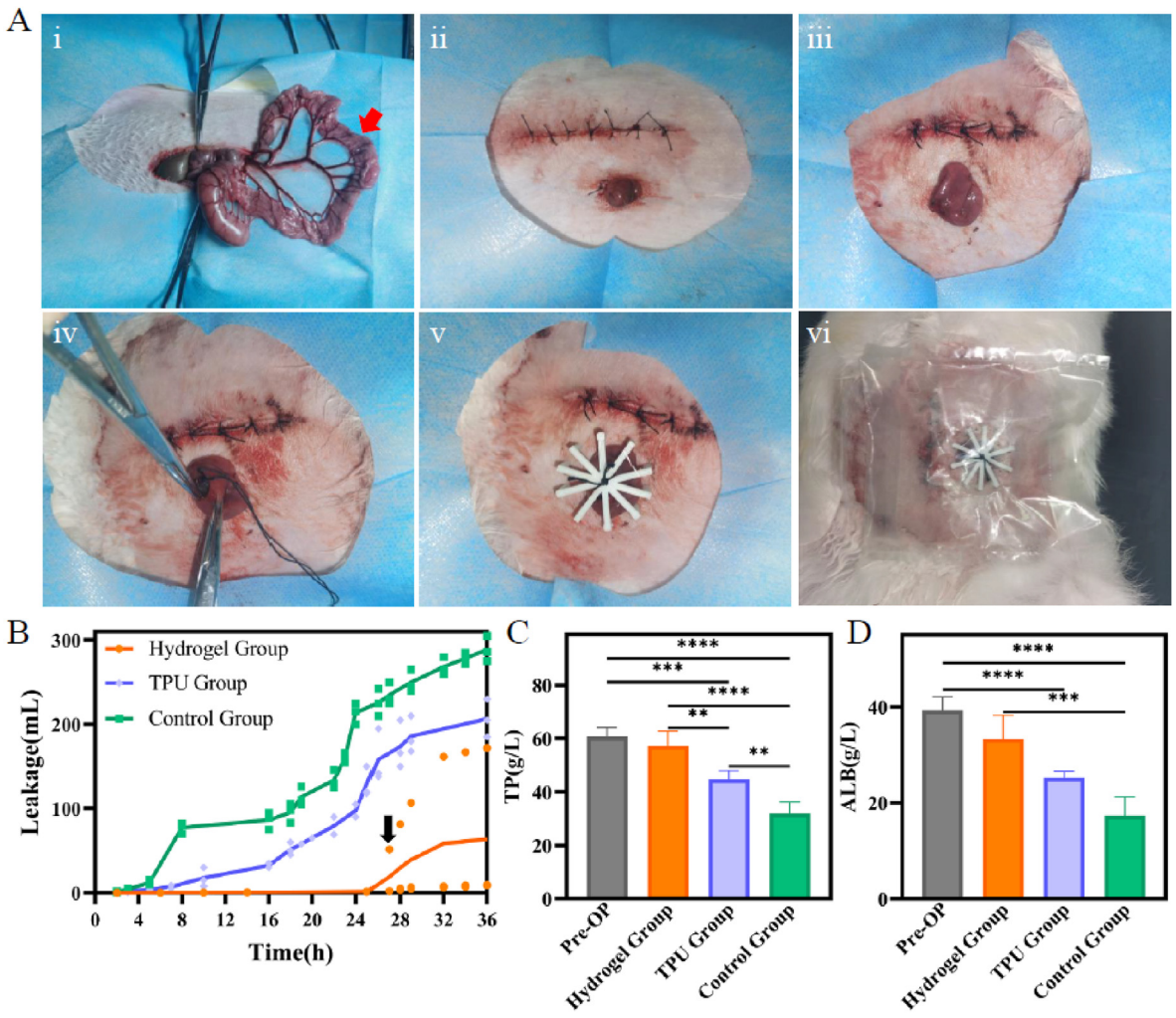

Fig. 8. Application of 4D-printed bilayer hydrogel in the EAFs of rabbits. (A) Surgical procedure and implantation of 4D-printed bilayer hydrogel stent: (i) Cut open abdomen along linea alba, and pull a section of ileum outside skin through a puncture in the left abdominal wall; Red arrow: surgical stoma location. (ii) Close abdominal wall, and suture the selected ileum to the abdomen; (iii) Cut the exposed ileum via a 2-cm incision to create an EAF model; (iv) Implant a 4D-printed bilayer hydrogel stent; (v) Fix the fistula stent outside abdomen with a 3D printed claw-shaped frame; (vi) Paste on ostomy bags to collect the leaked intestinal juice. (B) Line chart of intestinal juice leakage, black arrow: abscission of the hydrogel stent in one rabbit. (C) Total protein and (D) albumin of pre- and post-operation. **$p < 0.05$, ***$p < 0.001$, ****$p < 0.0001$, statistical analysis using one-way ANOVA.

Credit author statement

Guiwen Qu: Conceptualization, Methodology, Investigation, Validation, Formal analysis, Writing – original draft. **Jinjian Huang**: Conceptualization, Methodology, Investigation. **Ze Li**: Methodology, Investigation. **Yungang Jiang**: Methodology. **Ye Liu**: Formal analysis. **Kang Chen**: Investigation. **Ziyan Xu**: Validation. **Yun Zhao**: Methodology. **Guosheng Gu**: Methodology, Writing – review & editing. **Xiuwen Wu**: Conceptualization, Methodology, Writing – review & editing, Supervision. **Jianan Ren**: Resources, Conceptualization, Writing – review & editing, Supervision.

Declaration of competing interest

The authors declare that they have no known competing financial interests or personal relationships that could have appeared to influence the work reported in this paper.

Acknowledgment

This work was supported by Distinguished Scholars Foundation of Jiangsu Province (JCRCB2016006), Jiangsu Key Research and Development Plan (BE2021727), and General Program of Medical Research from the Jiangsu Commission of Health (M2020052).

References

[1] C. Terzi, T. Egeli, A.E. Canda, N.C. Arslan, Management of enteroatmospheric fistulae, Int. Wound J. 11 (Suppl 1) (2014) 17–21.
[2] S. Di Saverio, A. Tarasconi, D.A. Walczak, R. Cirocchi, M. Mandrioli, A. Birindelli, G. Tugnoli, Classification, prevention and management of entero-atmospheric fistula: a state-of-the-art review, Langenbeck's Arch. Surg. 401 (1) (2016) 1–13.
[3] A.R. Bhama, Evaluation and management of enterocutaneous fistula, Dis. Colon Rectum 62 (8) (2019) 906–910.
[4] S.K. Rasilainen, M. Viljanen, P.J. Mentula, A.K. Leppäniemi, Enteroatmospheric fistulae in open abdomen: management and outcome – single center experience, Int. J. Surgery Open 5 (2016) 44–49.
[5] S. Layec, E. Seynhaeve, F. Trivin, M. Carsin-Mahe, L. Dussaulx, D. Picot, Management of entero-atmospheric fistulas by chyme reinfusion: a retrospective study, Clin. Nutr. 39 (12) (2020) 3695–3702.
[6] L. Rebibo, A. Wacrenier, H. Thiebault, R. Delcenserie, J.-M. Regimbeau, Combined endoscopic and surgical covered stent placement: a new tailored treatment for enteroatmospheric fistula in patients with terminal ileostomy, Endoscopy 49 (S 01) (2017) E35–E36.
[7] G. Wang, J. Ren, S. Liu, X. Wu, G. Gu, J. Li, Fistula patch": making the treatment of enteroatmospheric fistulae in the open abdomen easier, J Trauma Acute Care Surg 74 (4) (2013) 1175–1177.
[8] L.E. Miranda, A.C. Miranda, Enteroatmospheric fistula management by endoscopic gastrostomy PEG tube, Int. Wound J. 14 (6) (2017) 915–917.

[9] M.T. Ozer, H. Sinan, N. Zeybek, Y. Peker, A simple novel technique for enteroatmospheric fistulae: silicone fistula plug, Int. Wound J. 11 (Suppl 1) (2014) 22–24.
[10] S. Di Saverio, S. Villani, A. Biscardi, E. Giorgini, G. Tugnoli, Open abdomen with concomitant enteroatmospheric fistula: validation, refinements, and adjuncts to a novel approach, J. Trauma 71 (3) (2011) 760–762.
[11] Z.Y. Xu, H.J. Ren, J.J. Huang, Z.A Li, J.A. Ren, Application of a 3D-printed "fistula stent" in plugging enteroatmospheric fistula with open abdomen: A case report, World J. Gastroenterol 25 (14) (2019) 1775–1782.
[12] J. Huang, H. Ren, Y. Jiang, X. Wu, J. Ren, Technique advances in enteroatmospheric fistula isolation after open abdomen: a review and outlook, Front Surg 7 (2020), 559443.
[13] Q. Gao, X. Niu, L. Shao, L. Zhou, Z. Lin, A. Sun, J. Fu, Z. Chen, J. Hu, Y. Liu, Y. He, 3D printing of complex GelMA-based scaffolds with nanoclay, Biofabrication 11 (3) (2019), 035006.
[14] A. Vedadghavami, F. Minooei, M.H. Mohammadi, S. Khetani, A. Rezaei Kolahchi, S. Mashayekhan, A. Sanati-Nezhad, Manufacturing of hydrogel biomaterials with controlled mechanical properties for tissue engineering applications, Acta Biomater. 62 (2017) 42–63.
[15] C. Wang, Y. Liu, X. Qu, B. Shi, Q. Zheng, X. Lin, S. Chao, C. Wang, J. Zhou, Y. Sun, G. Mao, Z. Li, Ultra-stretchable and fast self-healing ionic hydrogel in cryogenic environments for artificial nerve fiber, Adv. Mater. 34 (16) (2022), 2105416.
[16] D. Zhu, Z. Li, K. Huang, T.G. Caranasos, J.S. Rossi, K. Cheng, Minimally invasive delivery of therapeutic agents by hydrogel injection into the pericardial cavity for cardiac repair, Nat. Commun. 12 (1) (2021), 1412.
[17] C. Wang, X. Qu, Q. Zheng, Y. Liu, P. Tan, B. Shi, H. Ouyang, S. Chao, Y. Zou, C. Zhao, Z. Liu, Y. Li, Z. Li, Stretchable, self-healing, and skin-mounted active sensor for multipoint muscle function assessment, ACS Nano 15 (6) (2021) 10130–10140.
[18] Y. Gai, H. Li, Z. Li, Self-Healing functional electronic devices, Small 17 (41) (2021), 2101383.
[19] H. Li, X. Wang, W. Jiang, H. Fu, X. Liang, K. Zhang, Z. Li, C. Zhao, H. Feng, J. Nie, R. Liu, G. Zhou, Y. Fan, Z. Li, Alkali metal chlorides based hydrogel as eco-friendly neutral electrolyte for bendable solid-state capacitor, Adv. Mater. Interfac. 5 (10) (2018), 1701648.
[20] S. Sultan, A.P. Mathew, 3D printed scaffolds with gradient porosity based on a cellulose nanocrystal hydrogel, Nanoscale 10 (9) (2018) 4421–4431.
[21] B. Gao, Q. Yang, X. Zhao, G. Jin, Y. Ma, F. Xu, 4D bioprinting for biomedical applications, Trends Biotechnol. 34 (9) (2016) 746–756.
[22] J. Huang, S. Xia, Z. Li, X. Wu, J. Ren, Applications of four-dimensional printing in emerging directions: review and prospects, J. Mater. Sci. Technol. 91 (2021) 105–120.
[23] Q. Yang, B. Gao, F. Xu, Recent advances in 4D bioprinting, Biotechnol. J. 15 (1) (2020), 1900086.
[24] X. Kuang, D.J. Roach, J. Wu, C.M. Hamel, Z. Ding, T. Wang, M.L. Dunn, H.J. Qi, Advances in 4D printing: materials and applications, Adv. Funct. Mater. 29 (2) (2019), 1805290.
[25] S. Miao, N. Castro, M. Nowicki, L. Xia, H. Cui, X. Zhou, W. Zhu, S.J. Lee, K. Sarkar, G. Vozzi, Y. Tabata, J. Fisher, L.G. Zhang, 4D printing of polymeric materials for tissue and organ regeneration, Mater. Today 20 (10) (2017) 577–591.
[26] A. Kirillova, R. Maxson, G. Stoychev, C.T. Gomillion, L. Ionov, 4D biofabrication using shape-morphing hydrogels, Adv. Mater. 29 (46) (2017), 1703443.
[27] G.H. Yang, M. Yeo, Y.W. Koo, G.H. Kim, 4D bioprinting: technological advances in biofabrication, Macromol. Biosci. 19 (5) (2019), 1800441.
[28] S.H. Kim, Y.B. Seo, Y.K. Yeon, Y.J. Lee, H.S. Park, M.T. Sultan, J.M. Lee, J.S. Lee, O.J. Lee, H. Hong, H. Lee, O. Ajiteru, Y.J. Suh, S.-H. Song, K.-H. Lee, C.H. Park, 4D-bioprinted silk hydrogels for tissue engineering, Biomaterials 260 (2020), 120281.
[29] Y. Wang, H. Cui, Y. Wang, C. Xu, T.J. Esworthy, S.Y. Hann, M. Boehm, Y.L. Shen, D. Mei, L.G. Zhang, 4D printed cardiac construct with aligned myofibers and adjustable curvature for myocardial regeneration, ACS Appl. Mater. Interfaces 13 (11) (2021) 12746–12758.
[30] J. Wang, H. Gao, Y. Hu, N. Zhang, W. Zhou, C. Wang, B.P. Binks, Z. Yang, 3D printing of Pickering emulsion inks to construct poly(D,L-lactide-co-trimethylene carbonate)-based porous bioactive scaffolds with shape memory effect, J. Mater. Sci. 56 (1) (2021) 731–745.
[31] G. Le Fer, M.L. Becker, 4D printing of resorbable complex shape-memory poly(propylene fumarate) star scaffolds, ACS Appl. Mater. Interfaces 12 (20) (2020) 22444–22452.
[32] N. Maity, N. Mansour, P. Chakraborty, D. Bychenko, E. Gazit, D. Cohn, A personalized multifunctional 3D printed shape memory-displaying, drug releasing tracheal stent, Adv. Funct. Mater. 31 (50) (2021), 2108436.
[33] P. Lin, S. Ma, X. Wang, F. Zhou, Molecularly engineered dual-crosslinked hydrogel with ultrahigh mechanical strength, toughness, and good self-recovery, Adv. Mater. 27 (12) (2015) 2054–2059.
[34] S.Y. Zheng, H. Ding, J. Qian, J. Yin, Z.L. Wu, Y. Song, Q. Zheng, Metal-coordination complexes mediated physical hydrogels with high toughness, stick–slip tearing behavior, and good processability, Macromolecules 49 (24) (2016) 9637–9646.
[35] J. Huang, Y. Liu, X. Chi, Y. Jiang, Z. Xu, G. Qu, Y. Zhao, Z. Li, C. Chen, G. Chen, X. Wu, J. Ren, Programming electronic skin with diverse skin-like properties, J. Mater. Chem. A 9 (2) (2021).
[36] Y. Ma, M. Hua, S. Wu, Y. Du, X. Pei, X. Zhu, F. Zhou, X. He, Bioinspired high-power-density strong contractile hydrogel by programmable elastic recoil, Sci. Adv. 6 (47) (2020), eabd2520.
[37] Y.-Q. Wang, Y. Zhu, J.-H. Wang, X.-N. Li, X.-G. Wu, Y.-X. Qin, W.-Y. Chen, Fe3+, NIR light and thermal responsive triple network composite hydrogel with multi-shape memory effect, Compos. Sci. Technol. 206 (2021), 108653.
[38] R.M. Domingues, M.E. Gomes, R.L. Reis, The potential of cellulose nanocrystals in tissue engineering strategies, Biomacromolecules 15 (7) (2014) 2327–2346.
[39] J. Liu, F. Cheng, H. Grenman, S. Spoljaric, J. Seppala, E.E. J, S. Willfor, C. Xu, Development of nanocellulose scaffolds with tunable structures to support 3D cell culture, Carbohydr. Polym. 148 (2016) 259–271.
[40] S.D. Dutta, J. Hexiu, D.K. Patel, K. Ganguly, K.T. Lim, 3D-printed bioactive and biodegradable hydrogel scaffolds of alginate/gelatin/cellulose nanocrystals for tissue engineering, Int. J. Biol. Macromol. 167 (2021) 644–658.
[41] C. Calvino, N. Macke, R. Kato, S.J. Rowan, Development, processing and applications of bio-sourced cellulose nanocrystal composites, Prog. Polym. Sci. 103 (2020), 101221.
[42] T. Ma, L. Lv, C. Ouyang, X. Hu, X. Liao, Y. Song, X. Hu, Rheological behavior and particle alignment of cellulose nanocrystal and its composite hydrogels during 3D printing, Carbohydr. Polym. 253 (2021), 117217.
[43] J. Huang, Y. Deng, J. Ren, G. Chen, G. Wang, F. Wang, X. Wu, Novel in situ forming hydrogel based on xanthan and chitosan re-gelifying in liquids for local drug delivery, Carbohydr. Polym. 186 (2018) 54–63.
[44] A. Ding, O. Jeon, R. Tang, Y.B. Lee, S.J. Lee, E. Alsberg, Cell-laden multiple-step and reversible 4D hydrogel actuators to mimic dynamic tissue morphogenesis, Adv. Sci. 8 (9) (2021), 2004616.
[45] C. Ma, W. Lu, X. Yang, J. He, X. Le, L. Wang, J. Zhang, M.J. Serpe, Y. Huang, T. Chen, Bioinspired anisotropic hydrogel actuators with on-off switchable and color-tunable fluorescence behaviors, Adv. Funct. Mater. 28 (7) (2018), 1704568.
[46] J.J. Huang, J.A. Ren, G.F. Wang, Z.A. Li, X.W. Wu, H.J. Ren, S. Liu, 3D-printed "fistula stent" designed for management of enterocutaneous fistula: An advanced strategy, World J. Gastroenterol. 23 (41) (2017) 7489–7494.
[47] J. Qu, X. Zhao, Y. Liang, T. Zhang, P.X. Ma, B. Guo, Antibacterial adhesive injectable hydrogels with rapid self-healing, extensibility and compressibility as wound dressing for joints skin wound healing, Biomaterials 183 (2018) 185–199.
[48] L. Li, J. Ge, P.X. Ma, B. Guo, Injectable conducting interpenetrating polymer network hydrogels from gelatin-graft-polyaniline and oxidized dextran with enhanced mechanical properties, RSC Adv. 5 (112) (2015) 92490–92498.
[49] D.A. Lloyd, S.M. Gabe, A.C. Windsor, Nutrition and management of enterocutaneous fistula, Br. J. Surg. 93 (9) (2006) 1045–1055.